Biomedical Optics EXPRESS

In vivo human crystalline lens topography

Sergio Ortiz,[1*] Pablo Pérez-Merino,[1] Enrique Gambra,[1] Alberto de Castro,[1] and Susana Marcos[1]

[1]*Instituto de Óptica "Daza de Valdés", Consejo Superior de Investigaciones Científicas, C/Serrano 121, 28006 Madrid, Spain*

**sortiz@io.cfmac.csic.es*

Abstract: Custom high-resolution high-speed anterior segment spectral domain optical coherence tomography (OCT) was used to characterize three-dimensionally (3-D) the human crystalline lens *in vivo*. The system was provided with custom algorithms for denoising and segmentation of the images, as well as for fan (scanning) and optical (refraction) distortion correction, to provide fully quantitative images of the anterior and posterior crystalline lens surfaces. The method was tested on an artificial eye with known surfaces geometry and on a human lens *in vitro*, and demonstrated on three human lenses *in vivo*. Not correcting for distortion overestimated the anterior lens radius by 25% and the posterior lens radius by more than 65%. *In vivo* lens surfaces were fitted by biconicoids and Zernike polynomials after distortion correction. The anterior lens radii of curvature ranged from 10.27 to 14.14 mm, and the posterior lens radii of curvature ranged from 6.12 to 7.54 mm. Surface asphericities ranged from –0.04 to –1.96. The lens surfaces were well fitted by quadrics (with variation smaller than 2%, for 5-mm pupils), with low amounts of high order terms. Surface lens astigmatism was significant, with the anterior lens typically showing horizontal astigmatism (Z_2^2 ranging from –11 to –1 μm) and the posterior lens showing vertical astigmatism (Z_2^2 ranging from 6 to 10 μm).

OCIS codes: (110.4500) Optical coherence tomography; (120.6650) Surface measurements, figure; (120.4640) Optical instruments; (120.4800) Optical standards and testing; (110.6880) Three-dimensional image acquisition; (330.7327) Visual optics, ophthalmic instrumentation.

References and links

1. P. Kiely, G. Smith, and L. Carney, "The mean shape of the human cornea," Opt. Acta (Lond.) **29**(8), 1027–1040 (1982).
2. J. Schwiegerling, J. E. Greivenkamp, and J. M. Miller, "Representation of videokeratoscopic height data with Zernike polynomials," J. Opt. Soc. Am. A **12**(10), 2105–2113 (1995).
3. M. Dubbelman, H. A. Weeber, R. G. van der Heijde, and H. J. Völker-Dieben, "Radius and asphericity of the posterior corneal surface determined by corrected Scheimpflug photography," Acta Ophthalmol. Scand. **80**(4), 379–383 (2002).
4. A. Gullstrand, "Appendices to Part I," in *Helmholtz's Treatise on Physiological Optics* (Optical Society of America, Rochester, NY, 1924), pp. 350–358.
5. H. Helmholtz, "Ueber die accommodation des auges," Arch. Ophthal. **1**, 1–74 (1855).
6. A. Glasser and M. C. W. Campbell, "Presbyopia and the optical changes in the human crystalline lens with age," Vision Res. **38**(2), 209–229 (1998).
7. A. Glasser and P. L. Kaufman, "The mechanism of accommodation in primates," Ophthalmology **106**(5), 863–872 (1999).
8. G. Smith, B. K. Pierscionek, and D. A. Atchison, "The optical modelling of the human lens," Ophthalmic Physiol. Opt. **11**(4), 359–369 (1991).
9. L. F. Garner and M. K. Yap, "Changes in ocular dimensions and refraction with accommodation," Ophthalmic Physiol. Opt. **17**(1), 12–17 (1997).
10. L. F. Garner, "Calculation of the radii of curvature of the crystalline lens surfaces," Ophthalmic Physiol. Opt. **17**(1), 75–80 (1997).
11. A. Glasser and M. C. W. Campbell, "Biometric, optical and physical changes in the isolated human crystalline lens with age in relation to presbyopia," Vision Res. **39**(11), 1991–2015 (1999).

#170171 - $15.00 USD Received 7 Jun 2012; rev. 26 Jul 2012; accepted 24 Aug 2012; published 12 Sep 2012

12. F. Manns, V. Fernandez, S. Zipper, S. Sandadi, M. Hamaoui, A. Ho, and J. M. Parel, "Radius of curvature and asphericity of the anterior and posterior surface of human cadaver crystalline lenses," Exp. Eye Res. **78**(1), 39–51 (2004).
13. A. M. Rosen, D. B. Denham, V. Fernandez, D. Borja, A. Ho, F. Manns, J. M. Parel, and R. C. Augusteyn, "*In vitro* dimensions and curvatures of human lenses," Vision Res. **46**(6-7), 1002–1009 (2006).
14. Y. Sakamoto, K. Sasaki, Y. Nakamura, and N. Watanabe, "Reproducibility of data obtained by a newly developed anterior eye segment analysis system, EAS-1000," Ophthalmic Res. **24**(Suppl 1), 10–20 (1992).
15. C. A. Cook and J. F. Koretz, "Methods to obtain quantitative parametric descriptions of the optical surfaces of the human crystalline lens from Scheimpflug slit-lamp images. I. Image processing methods," J. Opt. Soc. Am. A **15**(6), 1473–1485 (1998).
16. M. Dubbelman and G. L. Van der Heijde, "The shape of the aging human lens: curvature, equivalent refractive index and the lens paradox," Vision Res. **41**(14), 1867–1877 (2001).
17. M. Dubbelman, G. L. van der Heijde, and H. A. Weeber, "The thickness of the aging human lens obtained from corrected Scheimpflug images," Optom. Vis. Sci. **78**(6), 411–416 (2001).
18. M. Dubbelman, G. L. Van der Heijde, and H. A. Weeber, "Change in shape of the aging human crystalline lens with accommodation," Vision Res. **45**(1), 117–132 (2005).
19. D. A. Goss, H. G. Van Veen, B. B. Rainey, and B. Feng, "Ocular components measured by keratometry, phakometry, and ultrasonography in emmetropic and myopic optometry students," Optom. Vis. Sci. **74**(7), 489–495 (1997).
20. P. Rosales, M. Dubbelman, S. Marcos, and R. van der Heijde, "Crystalline lens radii of curvature from Purkinje and Scheimpflug imaging," J. Vis. **6**(10), 5 (2006).
21. P. Rosales and S. Marcos, "Phakometry and lens tilt and decentration using a custom-developed Purkinje imaging apparatus: validation and measurements," J. Opt. Soc. Am. A **23**(3), 509–520 (2006).
22. P. Rosales, M. Wendt, S. Marcos, and A. Glasser, "Changes in crystalline lens radii of curvature and lens tilt and decentration during dynamic accommodation in rhesus monkeys," J. Vis. **8**(1), 18, 1–12 (2008).
23. J. E. Koretz, S. A. Strenk, L. M. Strenk, and J. L. Semmlow, "Scheimpflug and high-resolution magnetic resonance imaging of the anterior segment: a comparative study," J. Opt. Soc. Am. A **21**(3), 346–354 (2004).
24. P. Rosales and S. Marcos, "Pentacam Scheimpflug quantitative imaging of the crystalline lens and intraocular lens," J. Refract. Surg. **25**(5), 421–428 (2009).
25. A. S. Vilupuru and A. Glasser, "Dynamic accommodative changes in rhesus monkey eyes assessed with A-scan ultrasound biometry," Optom. Vis. Sci. **80**(5), 383–394 (2003).
26. C. E. Jones, D. A. Atchison, R. Meder, and J. M. Pope, "Refractive index distribution and optical properties of the isolated human lens measured using magnetic resonance imaging (MRI)," Vision Res. **45**(18), 2352–2366 (2005).
27. E. A. Hermans, P. J. Pouwels, M. Dubbelman, J. P. Kuijer, R. G. van der Heijde, and R. M. Heethaar, "Constant volume of the human lens and decrease in surface area of the capsular bag during accommodation: an MRI and Scheimpflug study," Invest. Ophthalmol. Vis. Sci. **50**(1), 281–289 (2009).
28. S. Kasthurirangan, E. L. Markwell, D. A. Atchison, and J. M. Pope, "MRI study of the changes in crystalline lens shape with accommodation and aging in humans," J. Vis. **11**(3), 19 (2011).
29. D. Huang, E. A. Swanson, C. P. Lin, J. S. Schuman, W. G. Stinson, W. Chang, M. R. Hee, T. Flotte, K. Gregory, C. A. Puliafito, and J. G. Fujimoto, "Optical coherence tomography," Science **254**(5035), 1178–1181 (1991).
30. I. Grulkowski, M. Gora, M. Szkulmowski, I. Gorczynska, D. Szlag, S. Marcos, A. Kowalczyk, and M. Wojtkowski, "Anterior segment imaging with Spectral OCT system using a high-speed CMOS camera," Opt. Express **17**(6), 4842–4858 (2009).
31. M. Gora, K. Karnowski, M. Szkulmowski, B. J. Kaluzny, R. Huber, A. Kowalczyk, and M. Wojtkowski, "Ultra high-speed swept source OCT imaging of the anterior segment of human eye at 200 kHz with adjustable imaging range," Opt. Express **17**(17), 14880–14894 (2009).
32. S. Ortiz, D. Siedlecki, L. Remon, and S. Marcos, "Three-dimensional ray tracing on Delaunay-based reconstructed surfaces," Appl. Opt. **48**(20), 3886–3893 (2009).
33. S. Ortiz, D. Siedlecki, L. Remon, and S. Marcos, "Optical coherence tomography for quantitative surface topography," Appl. Opt. **48**(35), 6708–6715 (2009).
34. M. C. M. Dunne, L. N. Davies, and J. S. Wolffsohn, "Accuracy of cornea and lens biometry using anterior segment optical coherence tomography," J. Biomed. Opt. **12**(6), 064023 (2007).
35. R. Yadav, K. Ahmad, and G. Yoon, "Scanning system design for large scan depth anterior segment optical coherence tomography," Opt. Lett. **35**(11), 1774–1776 (2010).
36. M. Shen, M. R. Wang, Y. Yuan, F. Chen, C. L. Karp, S. H. Yoo, and J. Wang, "SD-OCT with prolonged scan depth for imaging the anterior segment of the eye," Ophthalmic Surg. Lasers Imaging **41**(6 Suppl), S65–S69 (2010).
37. S. R. Uhlhorn, D. Borja, F. Manns, and J. M. Parel, "Refractive index measurement of the isolated crystalline lens using optical coherence tomography," Vision Res. **48**(27), 2732–2738 (2008).
38. E. Kim, K. Ehrmann, S. Uhlhorn, D. Borja, E. Arrieta-Quintero, and J. M. Parel, "Semiautomated analysis of optical coherence tomography crystalline lens images under simulated accommodation," J. Biomed. Opt. **16**(5), 056003 (2011).

#170171 - $15.00 USD Received 7 Jun 2012; rev. 26 Jul 2012; accepted 24 Aug 2012; published 12 Sep 2012

39. B. M. Maceo, F. Manns, D. Borja, D. Nankivil, S. Uhlhorn, E. Arrieta, A. Ho, R. C. Augusteyn, and J. M. Parel, "Contribution of the crystalline lens gradient refractive index to the accommodation amplitude in non-human primates: *in vitro* studies," J. Vis. **11**(13), 23 (2011).
40. A. de Castro, S. Ortiz, E. Gambra, D. Siedlecki, and S. Marcos, "Three-dimensional reconstruction of the crystalline lens gradient index distribution from OCT imaging," Opt. Express **18**(21), 21905–21917 (2010).
41. D. Borja, D. Siedlecki, A. de Castro, S. Uhlhorn, S. Ortiz, E. Arrieta, J. M. Parel, S. Marcos, and F. Manns, "Distortions of the posterior surface in optical coherence tomography images of the isolated crystalline lens: effect of the lens index gradient," Biomed. Opt. Express **1**(5), 1331–1340 (2010).
42. A. de Castro, S. Barbero, S. Ortiz, and S. Marcos, "Accuracy of the reconstruction of the crystalline lens gradient index with optimization methods from ray tracing and Optical Coherence Tomography data," Opt. Express **19**(20), 19265–19279 (2011).
43. A. de Castro, D. Siedlecki, D. Borja, S. Uhlhorn, J. M. Parel, F. Manns, and S. Marcos, "Age-dependent variation of the Gradient Index profile in human crystalline lenses," J. Mod. Opt. **58**(19-20), 1781–1787 (2011).
44. D. Siedlecki, A. de Castro, E. Gambra, S. Ortiz, D. Borja, S. Uhlhorn, F. Manns, S. Marcos, and J. M. Parel, "Distortion correction of OCT images of the crystalline lens: gradient index approach," Optom. Vis. Sci. **89**(5), E709–E718 (2012).
45. S. Ortiz, D. Siedlecki, P. Pérez-Merino, N. Chia, A. de Castro, M. Szkulmowski, M. Wojtkowski, and S. Marcos, "Corneal topography from spectral optical coherence tomography (sOCT)," Biomed. Opt. Express **2**(12), 3232–3247 (2011).
46. S. Ortiz, D. Siedlecki, I. Grulkowski, L. Remon, D. Pascual, M. Wojtkowski, and S. Marcos, "Optical distortion correction in optical coherence tomography for quantitative ocular anterior segment by three-dimensional imaging," Opt. Express **18**(3), 2782–2796 (2010).
47. M. Zhao, A. N. Kuo, and J. A. Izatt, "3D refraction correction and extraction of clinical parameters from spectral domain optical coherence tomography of the cornea," Opt. Express **18**(9), 8923–8936 (2010).
48. K. Karnowski, B. J. Kaluzny, M. Szkulmowski, M. Gora, and M. Wojtkowski, "Corneal topography with high-speed swept source OCT in clinical examination," Biomed. Opt. Express **2**(9), 2709–2720 (2011).
49. S. Ortiz, P. Pérez-Merino, N. Alejandre, E. Gambra, I. Jimenez-Alfaro, and S. Marcos, "Quantitative OCT-based corneal topography in keratoconus with intracorneal ring segments," Biomed. Opt. Express **3**(5), 814–824 (2012).
50. A. de Castro, P. Rosales, and S. Marcos, "Tilt and decentration of intraocular lenses *in vivo* from Purkinje and Scheimpflug imaging. Validation study," J. Cataract Refract. Surg. **33**(3), 418–429 (2007).
51. H. Farid and E. P. Simoncelli, "Differentiation of discrete multidimensional signals," IEEE Trans. Image Process. **13**(4), 496–508 (2004).
52. Y. Yang, K. Thompson, and S. A. Burns, "Pupil location under mesopic, photopic, and pharmacologically dilated conditions," Invest. Ophthalmol. Vis. Sci. **43**(7), 2508–2512 (2002).
53. T. Möller and J. F. Hughes, "Efficiently building a matrix to rotate one vector to another," J Graphics Tools **4**(4), 1–4 (1999).
54. H. Liou and N. A. Brennan, "Anatomically accurate, finite model eye for optical modelling," J. Opt. Soc. Am. A **14**(8), 1684–1695 (1997).
55. A. Pérez-Escudero, C. Dorronsoro, and S. Marcos, "Correlation between radius and asphericity in surfaces fitted by conics," J. Opt. Soc. Am. A **27**(7), 1541–1548 (2010).
56. J. Birkenfeld, A. de Castro, S. Ortiz, P. Pérez-Merino, E. Gambra, and S. Marcos, "Three-dimensional reconstruction of the isolated human crystalline lens gradient index distribution," Invest. Ophthalmol. Vis. Sci. **52**, E-Abstract 3404 (2011).
57. P. Artal, E. Berrio, A. Guirao, and P. Piers, "Contribution of the cornea and internal surfaces to the change of ocular aberrations with age," J. Opt. Soc. Am. A **19**(1), 137–143 (2002).
58. S. Barbero, S. Marcos, and J. Merayo-Lloves, "Corneal and total optical aberrations in a unilateral aphakic patient," J. Cataract Refract. Surg. **28**(9), 1594–1600 (2002).
59. J. E. Kelly, T. Mihashi, and H. C. Howland, "Compensation of corneal horizontal/vertical astigmatism, lateral coma, and spherical aberration by internal optics of the eye," J. Vis. **4**(4), 2 (2004).
60. S. Marcos, P. Rosales, L. Llorente, S. Barbero, and I. Jiménez-Alfaro, "Balance of corneal horizontal coma by internal optics in eyes with intraocular artificial lenses: evidence of a passive mechanism," Vision Res. **48**(1), 70–79 (2008).
61. E. Berrio, J. Tabernero, and P. Artal, "Optical aberrations and alignment of the eye with age," J. Vis. **10**(14), 34 (2010).
62. A. Roorda and A. Glasser, "Wave aberrations of the isolated crystalline lens," J. Vis. **4**(4), 1 (2004).
63. E. Acosta, J. M. Bueno, C. Schwarz, and P. Artal, "Relationship between wave aberrations and histological features in *ex vivo* porcine crystalline lenses," J. Biomed. Opt. **15**(5), 055001 (2010).

1. Introduction

The optical quality of the human eye is mainly determined by the geometrical and optical properties of two elements, cornea and crystalline lens. The cornea accounts for two-thirds of the optical refractive power, while the crystalline lens provides approximately one third of the

#170171 - $15.00 USD Received 7 Jun 2012; rev. 26 Jul 2012; accepted 24 Aug 2012; published 12 Sep 2012

total static refractive power of the eye, and it is the responsible for accommodation [1–10]. Accurate description of the geometry of the eye's optical components is critical for understanding their contribution to optical quality. Although the geometrical properties of the cornea have been widely studied due to its accessibility [1–3], accurate quantitative data of the crystalline lens geometry are limited to *in vitro* studies [11–13], while *in vivo* data are referred in most cases to axial properties (i.e. thickness) and central areas (i.e. central radius of curvature) [14–21].

The shape and alignment of the crystalline lens have been reported *in vivo* and *in vitro* using different imaging techniques. Radii of curvature, tilt and decentration of the lens have been measured using a Purkinje-imaging based method [20–22]. However, although Purkinje-based phakometry is a rapid, systematic, and reliable method, it does not provide the full geometry of the crystalline lens surfaces, nor a direct view of the lens. In contrast, Scheimpflug imaging allows acquisition of cross-sectional images of the crystalline lens, and with proper correction of the geometrical and optical distortions, the radii of curvature and asphericity of the lens surfaces can be obtained [16–18,23,24]. The slit-lamp configuration of Scheimpflug imaging-based systems (where the front view of the pupil appears superimposed to the cross-sectional image) frequently limits the view of the posterior lens. Besides, commercial Scheimpflug instruments, although providing images of the lens, are typically not corrected from optical distortion, preventing quantitative evaluation of lens parameters. To our knowledge, custom correction algorithms have only been applied to crystalline lens images in certain Scheimpflug instruments in a laboratory setting, and the reported crystalline lens parameters are restricted to a single cross-section of the lens [16,24]. In addition to optical techniques, the anterior chamber of the eye can be imaged through non-optical imaging techniques such as ultrasound [19,25] and Magnetic Resonance Imaging (MRI) [26–28]. These non-optical techniques allow visualization of the entire crystalline lens and its neighboring ocular structures. However, these are either invasive or time-consuming imaging methods, with significantly lower resolution than optical techniques, which impose major problems (low acquisition speed, motion artifacts or low sampling density) which prevent quantifying the crystalline lens geometry with high accuracy.

To our knowledge, the 3-D structure of the crystalline lens has not been investigated quantitatively with any method, likely as a result of the associated problems of the imaging techniques used to image the crystalline lens. Optical coherence tomography (OCT) is a high-resolution noncontact advanced optical imaging technique capable of providing 3-D evaluation of the anterior segment of the eye [29–33]. Several geometrical crystalline lens parameters surfaces have been reported previously with OCT, such as lens thickness and anterior and posterior lens radius of curvature in the horizontal meridian [34–36]. In addition, OCT has been used recently to quantify the crystalline lens shape in 2-D in human and primate lenses *in vitro* [37–39], and to estimate the Gradient Index (GRIN) distribution (from the optical distortion produced by GRIN on the posterior lens surface) in the porcine lens in 3-D and the human lens in 2-D [40–44].

Imaging the crystalline lens with sOCT poses some challenges: (1) The axial imaging range is limited by the resolution of the spectrometer, and this can be insufficient to image the entire anterior segment (from the anterior cornea to the posterior lens) in a single acquisition [30]. (2) Motion artifacts can limit the repeatability of the measurements, making it necessary to reduce acquisition time [45]; (3) Fan (arising from the scanning architecture) and optical (refraction) distortions, if left uncorrected, prevent quantitative analysis of the crystalline lens images [45–49].

In this study we measured and quantified the crystalline lens surface in 3-D. Further developments of the methods that we had previously developed and applied to achieve quantitative corneal topography [45,46,49] were applied to the quantification of the crystalline lens, overcoming limitations (2) and (3). Newly developed methods for registration and

#170171 - $15.00 USD Received 7 Jun 2012; rev. 26 Jul 2012; accepted 24 Aug 2012; published 12 Sep 2012

merging of sOCT images at different focus allowed full anterior segment imaging, overcoming limitation (1).

Accurate measurement of the lens geometry is crucial in the understanding of crystalline lens optical properties, and of the physical changes of the lens in accommodation and presbyopia, as well as in the design and evaluation of accommodation-restoration solutions for presbyopia, and to increase the predictability of intraocular lens implantation procedures.

In this study, we present the capability of sOCT imaging to provide 3-D parameters of the anterior and posterior lens surfaces (radii and asphericity) and lens thickness. To our knowledge, this is the first report of 3-D elevation maps of the anterior and posterior lens surfaces of the eye *in vivo*.

2. Material and Methods

2.1. Experimental sOCT setup

Images were collected using a custom-developed spectral OCT system (from a collaborative effort with Copernicus University, Torun, Poland) [30]. The setup is based on a fiber-optics Michelson interferometer configuration with a superluminescent diode (SLD) (λ_0 = 840 nm, $\Delta\lambda$ = 50 nm) as a light source, and a spectrometer (volume diffraction grating, and a 12-bit 4096-pixel line-scan CMOS camera) as a detector. The effective acquisition speed is 25000 A-Scans/s, which optimized balance between speed and SNR. The axial range of the instrument is 7 mm, resulting in a theoretical axial pixel resolution of 3.4 μm. The axial resolution predicted by the bandwidth of the SLD laser source is 6.9 μm.

2.2. Validation experiments on samples in vitro

The accuracy of the method to retrieve the shape of the lens was tested on a physical water cell model eye and on a donor lens.

The physical model eye has been described in previous studies where it was used to assess the accuracy of measurements of lens tilt and decentration from Scheimpflug and Purkinje imaging [50] and of topographic measurements with a Time Domain OCT system [46]. The water cell model consists of a PMMA cornea and a spherical biconvex intraocular lens with known spherical radii, as measured by a non-contact profilometer (PLu, Sensofar, Barcelona Spain), filled with saline solution. The index of refraction of the materials (1.486 for the artificial cornea and lens and 1.336 for the saline solution) were provided by the manufacturers. Measurements on the physical model eye were obtained with the SLD power exposure fixed at 800 μW. Each set of 3-D measurements was acquired in 0.72 seconds, similar to acquisition time used in *in vivo* eyes, with two acquisitions at two different planes of focus. Measurements were collected on a 10 × 15 mm zone, using 50 B-Scans composed by a collection of 360 A-Scans, providing a resolution of 0.04 mm for horizontal and 0.2 mm for vertical meridian.

Experiments were also performed on one crystalline lens from a 65-year donor eye, within 24 hours post-mortem (Eye Bank Transplant Services Foundation, Barcelona, Spain). Protocols for human tissue handling followed the guidelines of the Declaration of Helsinki, and had been approved by the Institutional Review Boards. Crystalline lens was extracted immediately before measurements and immersed in preservation medium (DMEM/F-12, D8437, Sigma, St. Louis, MO) at 25°C. The imaging procedure of the crystalline lens *in vitro* was similar to that described by de Castro et al. [40]. Images were acquired with the lens in two orientations, first with the anterior surface facing the OCT beam, “anterior up”, and then with the posterior surface facing the OCT beam (“posterior up”), after carefully flipping the lens. A homogeneous lens index of refraction of 1.413 was assumed in the calculations. Each single 3-D collection consisted of 70 B-scans with 1668 A-scans, with a lateral range of 12x12 mm, providing a resolution of 170x7 μm. The acquisition time of a full 3-D image was 4.5 s.

#170171 - $15.00 USD Received 7 Jun 2012; rev. 26 Jul 2012; accepted 24 Aug 2012; published 12 Sep 2012

2.3. Experimental protocols for anterior segment image acquisition in vivo

Images were collected on the right eye of 3 young subjects (ages 28-33). The subjects were considered healthy in a clinical ophthalmological examination. Refractions ranged between 0 to −4.75 D sphere and 0 to 1 D of cylinder. All protocols for the measurements *in vivo* had been approved by Institutional Review Boards. The subjects signed informed consents after the nature of the study had been explained, in accordance to the tenets of the Declaration of Helsinki. Measurements were performed under mydriasis (by Tropicamide 1%). The subjects were stabilized using a bite bar. Alignment of the subject was achieved with respect to the anterior corneal specular reflection, while the subject fixated on a reference maltese cross target projected on a minidisplay at optical infinity.

A total of 15 sets of 3-D data were collected in each eye: 5 repeated images of the cornea, 5 repeated images of the anterior part the lens, and 5 repeated images of the posterior part of the lens. All 3-D sets of data contained also the iris.

The SLD power exposure was fixed at 800 μW [45]. Focus was changed by an automatic displacement to achieve optimal imaging of the different anterior segment structures (cornea, anterior and posterior lens). Images of each axial region were collected in 0.72 s, in order to minimize the impact of motion artifacts. Measurements were collected on a 10 × 15 mm zone, using 50 B-Scans composed by a collection of 360 A-Scans, providing a resolution of 0.04 mm for horizontal and 0.2 mm for vertical meridian.

2.4. 3-D image analysis: denoising, segmentation, merging, distortion correction and surface fitting

In previous works corneal elevation maps from normal and pathological subjects were obtained using sOCT and analyzed using dedicated algorithms for volumetric data extraction [49]. The current study incorporates improvements in the processing algorithms (including a more sensitive automatic surface segmentation, resulting in a significant reduction of the detection noise, and a new implementation of Delaunay decomposition-based method for 3-D ray tracing and optical distortion correction methods), as well as new routines specifically developed for the requirements of the current application. The new algorithms include routines for: automatic detection of the pupil center and radius, estimation of the pupil plane orientation, and 3-D automatic merging of anterior segment images collected at different depths. The image processing algorithm can be summarized in nine steps. Only dedicated new routines are described in detail:

(1) Denoising: A rotational kernel transform was performed for an edge-preserving denoising, using a mask of size 9 pixels [49]. In addition, a wavelet low-pass filtering processing based on log-Gabor wavelet was used for 7 scales and 6 orientations.

(2) Statistical thresholding: An adaptive algorithm based on a multimodal Gaussian fitting of the histogram intensity (in a non-linear least squares sense) was performed on the entire 3-D sets of data, which allowed identifying a noise class from the signal.

(3) Volume clustering: The statistics of the noise and signal are overlapped. As a result, small randomly distributed volumes are mixed with the large volumes representing the objects of interest in 3-D (cornea, iris, lens surfaces, etc…). The number of pixels belonging to certain a volume is obtained by means of the connectivity of points. The volumes of interest are obtained by thresholding the number of elements according to the expected total number. Figure 1(a) shows examples of the volumes clustered in each of the 3-D data set collected at different depths: (a) cornea and iris, (b) anterior lens and iris, (c) posterior lens and iris.

(4) Multilayer segmentation: A new approach for automatic segmentation was developed, based on Canny detection in each A-scan (1-D signals). In an initial step, a Gaussian filter (standard deviation $\sigma = 5$ pixels) was convolved with the signal to reduce spurious peaks associated to noise detection in the CMOS line-camera. The first derivatives of the signal were then obtained by convolving the resultant A-Scan with finite-size linear-phase separable

#170171 - $15.00 USD Received 7 Jun 2012; rev. 26 Jul 2012; accepted 24 Aug 2012; published 12 Sep 2012

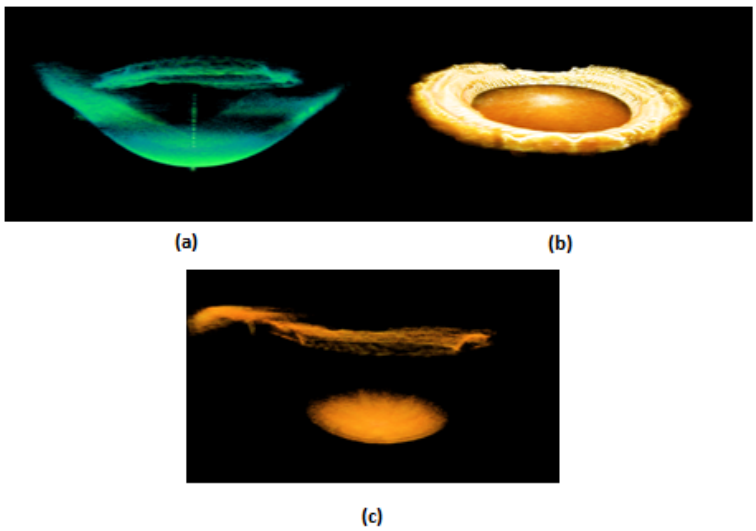

Fig. 1. Illustration of the three acquisitions of an individual data collection in subject S#1. (a) cornea and iris; (b) anterior lens and iris; (c) posterior lens and iris.

kernels for differentiation of the discrete data (A-Scan) [51]. The size of the kernels (3-9 pixels) controls the sensitivity of the algorithm to noise (the lower the number of pixels used for the kernel the higher the noise sensitivity). The result of the first derivative calculation provides both local maxima and minima of the A-scan. Maxima are identified by subtraction of the slope sign of two consecutive points (positive values). The number of local maxima is further reduced by thresholding the signal and removing the peaks below a certain value (set to the average of the signal plus a variable amount, in this case, 0.25 times the standard deviation of the signal). The maxima identified in the A-scans are connected in the 2-D cross-sections (B-scans) or in the 3-D data sets using the same neighborhood algorithm used for clustering, therefore allowing to segment layers. Figure 2 shows the application of developed routine to the segmentation of the anterior and posterior surface of the cornea. Figure 2(a) shows a typical raw A-scan (in black), the smoothed signal after application of a Gaussian (σ = 5) filter (in blue), and the identified local maxima (obtained by the application of the first derivative with a kernel of 9 pixels, red asterisks). Figure 2(b) illustrates the estimation of the maxima (red points) in a collection of A-scans in the cornea, and the identified layers for the

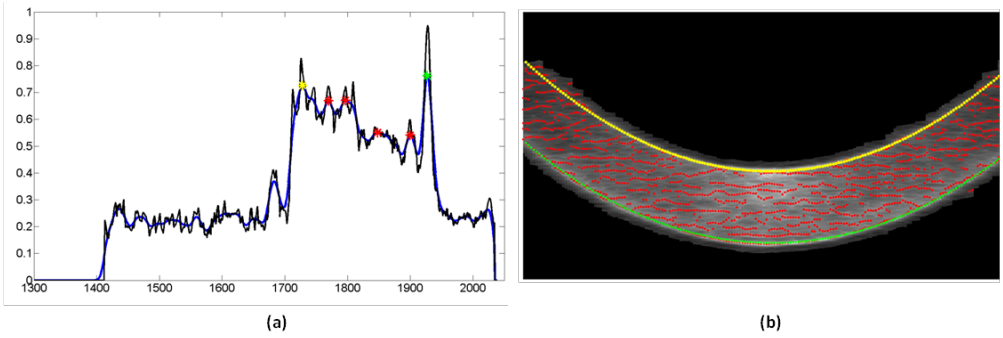

Fig. 2. (a) Illustration of the algorithm for maxima detection: Original A-Scan black; Filtered signal by Gaussian filtering, blue; Detected local maxima (red asterisks) by First derivative 9-pixel kernel computation. The anterior and posterior corneal peaks are marked by green and yellow asterisks, respectively. (b) Detection of maxima in corneal B-Scan (in red), and multilayer segmentation of the anterior surface (green line) and posterior surface (yellow line) by the neighborhood algorithm.

#170171 - $15.00 USD Received 7 Jun 2012; rev. 26 Jul 2012; accepted 24 Aug 2012; published 12 Sep 2012

anterior and posterior cornea surfaces (in green and yellow, respectively), following the application of the neighborhood algorithm.

(5) Pupil center reference: The pupil center was used as a reference across measurements (i.e. cornea, anterior and posterior lens) and to define the optical zone (effective area within the pupil). According to previous studies [52], the pupil center shifts little across pupil sizes and light conditions. In a previous work [49] we estimated the pupil center and optical zone by fitting the outer edge of pupil in 2-D en face images (computed by adding all images of a 3-D data set) to an ellipse. However, the current application requires 3-D position of the pupil center (including the axial coordinate), and estimation of the pupil plane in 3-D, as this information is used for registration and merging of the corneal and lens images. In this study, the lateral pupil coordinates were obtained as in the previous study [49], while the axial coordinate was obtained by nonlinear least-square fitting of the iris plane in 3-D (and evaluation of the plane at the estimated pupil lateral coordinates). In addition, the characteristic vector of the iris plane was obtained, which provided the tilt angle of this plane with respect to the OCT coordinate system.

(6) Merging 3-D volumes: The pupil coordinates are assumed as a common reference for the images of the anterior segment collected at different depths. Variations in the pupil diameter were negligible across images. Images of the cornea, anterior and posterior lens were merged using the pupil center and pupil plane orientation for registration. In a first step prior to merging, the corneal image was inverted, as for efficiency in the focus range shift, the cornea was acquired in the opposite side of the Fourier transform (in comparison with the crystalline lens acquisition). The 3-D volumes of the anterior cornea/iris and posterior lens/iris are shifted to the pupil center reference, and rotated (using a rotation matrix [53]) in order to superimpose the characteristic vectors of the corresponding pupil plane to those of the anterior lens/iris [53]. Figure 3 (Media 1) illustrates the process to obtain the full anterior segment 3-D image merging from the three volumetric acquisitions. A full overlapping of the iris from the 3 sets of images can be observed.

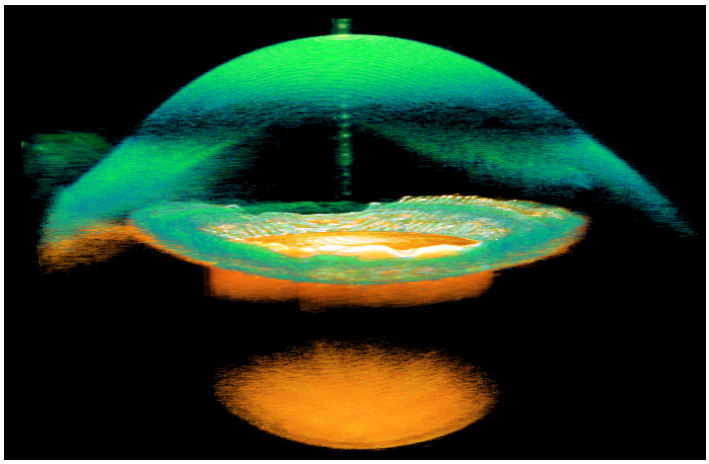

Fig. 3. (Media 1). Illustration of the merging of three volumetric acquisitions to obtain a 3-D full anterior segment image.

(7) Geometrical distances calculation and further denoising: The registration of the 3-D volumetric data sets involved shift and rotation by coordinates in optical distances, which actually differ across the different depths. Estimation of the geometrical parameters from the full anterior segment images (still subject of fan and optical distortion) required re-sampling of the surfaces in a rectangular equally distributed mesh of 100 x 100 points in the rectangle circumscribed by the pupil ellipse, as well as interpolation. The interpolation method was based on Delaunay description of the surfaces [32], and the use of radial base cubic functions

#170171 - $15.00 USD Received 7 Jun 2012; rev. 26 Jul 2012; accepted 24 Aug 2012; published 12 Sep 2012

(as those functions do not require the use of a regular grid of sampling without compromising accuracy). The interpolated coordinates are obtained from the nodes of the triangle elements that tile the surfaces in the Delaunay description. The procedure was performed for the four surfaces of the anterior segment: anterior-posterior cornea and anterior-posterior lens. The optical distance can be then calculated by direct subtraction of the coordinates of the different surfaces, while the geometrical distances were obtained by dividing the optical distance by the corresponding group refractive index at the illumination wavelength. The corneal refractive index was taken as 1.376, the aqueous humor refractive index as 1.336, and the crystalline lens refractive index was obtained from the age-dependent average refractive index expression derived by Uhlhorn et al. [37] (1.4176-1.4186 for the subjects of our study). The sampled anterior segment elevation data from anterior and posterior surfaces of the cornea and the lens were denoised using a fitting Zernike modal expansion (55 terms, 10th order). This iterative method allows further rejection of spurious points in the surface due to detection process.

(8) Distortion corrections: In order to correct the interface layers for the effect of distortion in general (fan distortion and refraction), it is required to propagate the geometrical distances obtained from the previous point along the directional cosines of the ray, taking into account the refraction that occurs at each interface between two media of different refractive indices [46]. A procedure similarly to that described in an earlier publication [49] and practically applied to the cornea was followed, expanding it sequentially from the cornea to the posterior surface of the crystalline lens. Correction of the fan and optical distortions produces large geometrical changes in the anterior optical surfaces, which are qualitatively observable in the diameter of the visible areas of the anterior, and to a larger extent, of the posterior lens. Figure 4 (Media 2) shows the difference in the segmented surfaces fully corrected from optical distortion correction (in green), and the segmented surfaces corrected from fan distortion but not from refraction effect (dividing only by its refractive index, in red).

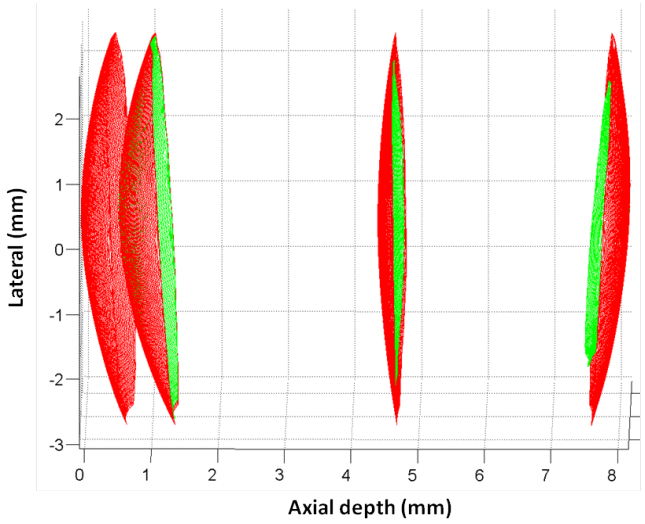

Fig. 4. (Media 2) Illustration of the effect of optical (refraction) correction (in green), in comparison with the correction of the surfaces by simple division by their corresponding refractive indices in an anterior segment image (in red). From left to right: segmented anterior and posterior corneal surfaces, and anterior and posterior lens surfaces.

(9) Surface fitting by quadrics (biconicoid, conicoid), and elevation maps: The surfaces were fitted by quadrics in a 5-mm of diameter optical zone with respect to their apexes. The corneal shape descriptive parameters (radii of curvature R_x and R_y and conic constants Q_x and Q_y) were obtained by biconic fitting. In addition, surfaces were also fitted by conicoids (defined by the radius of curvature R and conic constants Q). The elevation maps for the

#170171 - $15.00 USD Received 7 Jun 2012; rev. 26 Jul 2012; accepted 24 Aug 2012; published 12 Sep 2012

anterior and posterior lens after fan distortion correction only, and after full distortion correction and geometrical distances were represented as the difference of elevation data from the reference sphere, where warm colors represent points that are higher than the reference surface and cool colors represent points below the reference. The difference maps between the surfaces obtained with full correction and dividing the optical distances by the refractive indices were calculated by direct subtraction of the elevation maps, fitted to a Zernike expansion (55 terms, 10th order) within the same optical zone. The maps were represented using the so called "jet" color map in Matlab notation, where warm colors depict high differences while cold colors depict low differences. Thickness maps of the lens were obtained by direct subtraction of the anterior elevation map from the posterior, as for the full corrected lens as for the optical distances divided by refractive index one. The maps were represented using the so called "jet" color map in Matlab notation, where warm colors depict a thicker areas while cold colors depict thinner areas All maps were displayed in a square grid of 100x100 points in a 5-mm of diameter, with respect to the pupil center.

3. Results

3.1. In vitro samples

The images obtained from the physical model eye were processed using the developed image analysis and distortion correction algorithms. Table 1 shows the nominal radii of curvature of the cornea and lens surfaces in the model eye, along with the values before and after application of optical distortion correction algorithms. Fan distortion correction was applied in all cases. Discrepancies in the retrieved radii of curvature were 7.5% for the posterior cornea, 9.7% for the anterior lens and as high as 23.5% for the posterior lens. The accuracy in the radius of curvature retrieval increased dramatically after optical distortion correction, with discrepancies of 0.3% for the anterior cornea, 2.0% for the posterior cornea, 1.4% for the anterior lens, and 2.8% for the posterior lens.

Table 1. Surface radii of curvature from sphere fittings in the model eye: nominal values, values estimated from OCT measurements before and after correction of optical distortion.

	Cornea			**Lens**		
	Nominal (mm)	*OCT Uncorrected (mm)*	*OCT Corrected (mm)*	*Nominal (mm)*	*OCT Uncorrected (mm)*	*OCT Corrected (mm)*
Anterior	7.80	7.77	7.77	17.29	18.96	17.05
Posterior	6.48	6.96	6.35	11.04	13.64	10.74

The images obtained from the donor lens *in vitro* were processed using the developed image analysis and distortion correction algorithms. Figure 5 shows the elevation maps obtained of the posterior surface of a donor lens *in vitro* (direct view of the posterior lens, view of posterior lens distorted by the anterior lens, and posterior lens corrected from optical distortion by the anterior lens). Optical distortion correction decreases the error in the retrieved posterior lens radius of curvature from 8.23% to 0.9%. Correction also decreased the discrepancies in the RMS surface elevation map (referred to the best fitted sphere) from 48.3% (no optical distortion correction) to 4.5% (after optical distortion).

#170171 - $15.00 USD Received 7 Jun 2012; rev. 26 Jul 2012; accepted 24 Aug 2012; published 12 Sep 2012

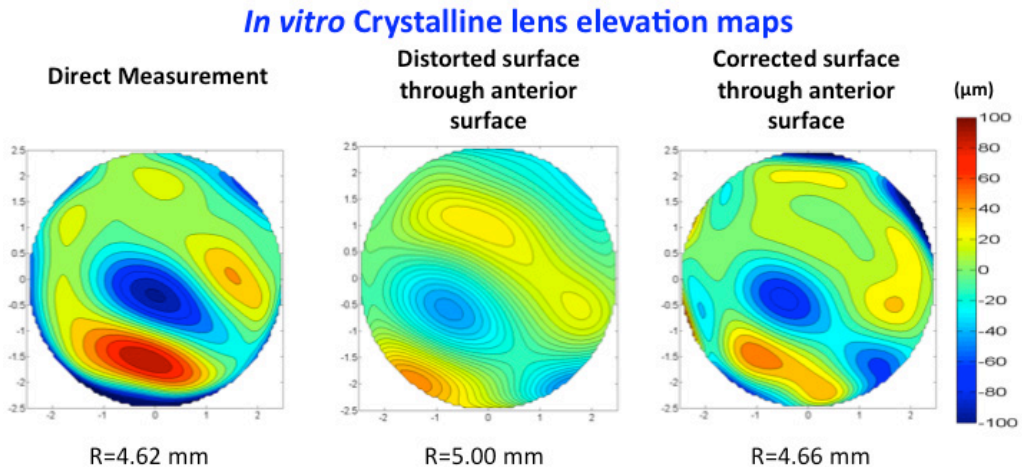

Fig. 5. Quantitative elevation maps of the posterior lens surface for the *in vitro* 65-year donor lens. Left panel: Measurements with the posterior surface of the lens facing the OCT beam ("posterior up"); Middle panel: Measurement of the posterior surface of the lens viewed through the anterior surface of the lens, and no optical distortion correction (simple division by the index of refraction); Left panel: Measurement of the posterior surface of the lens viewed through the anterior surface of the lens, after application of optical distortion correction Maps are Zernike fits to the elevation maps, relative to the best fitting sphere. R = radii of curvature of the best fitting sphere (from fits to sphere quadrics).

3.2. Cornea shape parameters

Corneal surface quantification is necessary to provide accurate optical distortion correction of the lens surfaces. Table 2 summarizes the anterior and posterior corneal parameters in the 3 subjects of the study after full distortion corrections, obtained from conicoid and biconicoid fittings of corneal surfaces in a 5-mm diameter zone.

Table 2. Radii of curvature and asphericity (Q-value) of the anterior and posterior cornea from biconicoid and conicoid fittings

	Radius of curvature					
	Anterior Cornea			**Posterior Cornea**		
	Biconicoid		***Conicoid***	***Biconicoid***		***Conicoid***
	Rx (mm)	*Ry (mm)*	*R (mm)*	*Rx (mm)*	*Ry (mm)*	*R (mm)*
S#1	7.40 ± 0.07	7.53 ± 0.03	7.47 ± 0.05	6.76 ± 0.13	6.59 ± 0.07	6.69 ± 0.10
S#2	7.95 ± 0.06	7.82 ± 0.10	7.87 ± 0.11	6.96 ± 0.07	6.95 ± 0.11	6.96 ± 0.08
S#3	7.47 ± 0.05	7.42 ± 0.14	7.43 ± 0.09	6.93 ± 0.06	6.70 ± 0.13	6.72 ± 0.11
	Asphericity (Q-Value)					
	Qx	*Qy*	*Q*	*Qx*	*Qy*	*Q*
S#1	0.10 ± 0.01	–0.19 ± 0.05	0.01 ± 0.04	–0.03 ± 0.05	0.06 ± 0.08	–0.01 ± 0.09
S#2	0.20 ± 0.05	–0.18 ± 0.08	0.10 ± 0.03	0.03 ± 0.05	0.01 ± 0.11	0.04 ± 0.03
S#3	0.11 ± 0.06	–0.02 ± 0.09	–0.01 ± 0.07	–0.08 ± 0.04	0.01 ± 0.03	0.01 ± 0.08

3.3. Effects of optical distortion on crystalline lens shape

To quantify the effect of optical distortion from preceding surfaces on the crystalline lens shape, we evaluated difference maps, obtained as the subtraction of the elevation map estimated after full optical correction from the map obtained after fan distortion correction and a simple division of the optical distances by the refractive indices, both for the anterior and posterior lens surface. Not correcting for optical distortion produced discrepancies ranging from 0 µm (in the center of the lens) up to 50 µm in the periphery of the anterior lens surface, and up to 200 µm in the periphery of the posterior lens. The difference maps (Fig. 6) reveal the progressive overestimation of the lens curvatures in the non-corrected maps. Although

#170171 - $15.00 USD Received 7 Jun 2012; rev. 26 Jul 2012; accepted 24 Aug 2012; published 12 Sep 2012

dominated by the differences in curvature, slight irregularities in the difference maps indicate the effect of optical distortion in astigmatism and other higher order terms.

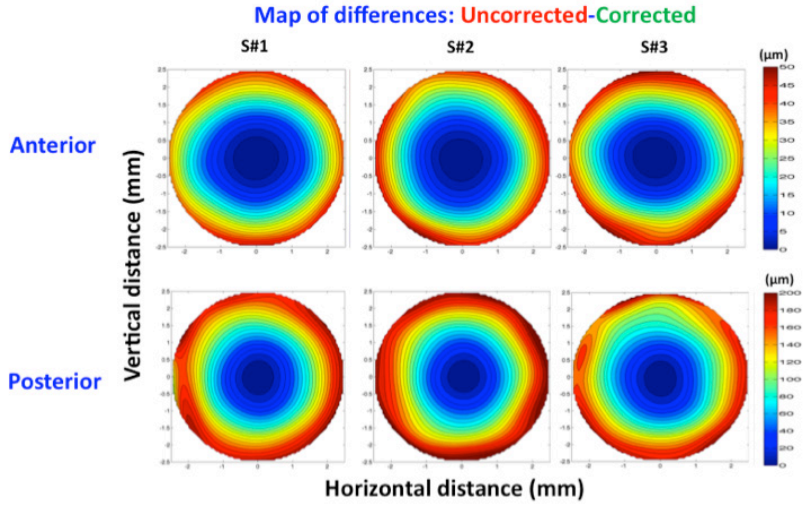

Fig. 6. Difference lens anterior (top) and posterior (bottom) elevation maps after optical distortion correction relative to elevation maps obtained by simple division of the optical distances by their corresponding refractive indices. Data are for 5-mm pupils.

3.4. Crystalline lens shape

Lens surfaces radii and asphericities (with and without optical distortion corrections) were obtained from OCT images obtained *in vivo* in three subjects, from conicoid and biconicoid fits to the retrieved surfaces (within 5-mm diameter zones). Data in Table 3 represent averages (and standard deviations) of 3 repeated measurements on each eye. Not correcting for optical distortion produced a systematic overestimation of the lens radii of curvature (Table 2), between 20.46 and 22.77% for the horizontal meridian, and between 20.96 and 32.81% for the vertical meridian (in the anterior lens), and between 63.40 and 72.70% for the horizontal meridian, and between 68.14 and 80.27% for the vertical meridian (in the posterior lens). For a conic fit, radii were overestimated between 20.20 and 23.56% in the anterior lens, and between 69.28 and 78.72% in the posterior lens.

Table 3. Radii of curvature from biconicoid and conicoid fits of the uncorrected and optical distortion corrected crystalline lens surfaces ***in vivo***

		Anterior Lens			**Posterior Lens**		
		Biconicoid		***Conicoid***	***Biconicoid***		***Conicoid***
		Rx (mm)	*Ry (mm)*	*R (mm)*	*Rx (mm)*	*Ry (mm)*	*R (mm)*
S#1	Uncorrected	17.36 ± 0.11	13.95 ± 0.21	15.42 ± 0.19	11.64 ± 0.01	13.51 ± 0.22	12.48 ± 0.11
	Corrected	14.14 ± 0.13	11.24 ± 0.30	12.48 ± 0.20	6.74 ± 0.11	7.54 ± 0.20	7.25 ± 0.25
S#2	Uncorrected	13.83 ± 0.07	13.64 ± 0.24	13.74 ± 0.09	10.06 ± 0.26	10.66 ± 0.29	10.36 ± 0.20
	Corrected	11.47 ± 0.09	10.27 ± 0.29	11.43 ± 0.04	6.10 ± 0.12	6.34 ± 0.04	6.12 ± 0.15
S#3	Uncorrected	15.60 ± 0.04	13.79 ± 0.38	14.64 ± 0.21	11.52 ± 0.12	13.43 ± 0.23	12.85 ± 0.04
	Corrected	12.95 ± 0.12	11.40 ± 0.19	12.18 ± 0.06	7.04 ± 0.12	7.45 ± 0.16	7.19 ± 0.03

Lens asphericities (Table 4) were negative in all eyes, although values differed significantly across subjects. While optical distortion correction modified the asphericity

#170171 - $15.00 USD Received 7 Jun 2012; rev. 26 Jul 2012; accepted 24 Aug 2012; published 12 Sep 2012

parameter, there was not a consistent trend toward overestimation or understimation without correction.

Table 4. Asphericity (Q-value) from biconicoid and conicoid fits of the uncorrected and optical distortion corrected crystalline lens surfaces

		Anterior			Posterior		
		Biconicoid		***Conicoid***	***Biconicoid***		***Conicoid***
		Qx	*Qy*	*Q*	*Qx*	*Qy*	*Q*
S#1	Uncorrected	–0.40 ± 0.34	–0.33 ± 0.12	–6.02 ± 0.03	–0.09 ± 0.06	–0.49 ± 0.11	–0.67 ± 0.25
	Corrected	–0.41 ± 0.15	–0.36 ± 0.20	–2.57 ± 0.31	–1.87 ± 0.93	–1.96 ± 0.76	–1.64 ± 0.33
S#2	Uncorrected	–0.33 ± 0.37	–0.42 ± 0.32	–0.29 ± 0.07	–0.45 ± 0.33	–0.24 ± 0.20	–0.66 ± 0.16
	Corrected	–0.40 ± 0.16	–0.26 ± 0.29	–0.43 ± 0.21	–0.06 ± 0.02	–0.09 ± 0.07	–0.01 ± 0.00
S#3	Uncorrected	–0.35 ± 0.41	–0.23 ± 0.20	–1.21 ± 0.43	–0.40 ± 0.10	–0.25 ± 0.23	–0.84 ± 0.22
	Corrected	–0.19 ± 0.23	–0.25 ± 0.32	–0.93 ± 0.40	–0.46 ± 0.22	–0.07 ± 0.08	–0.59 ± 0.07

3.5. Crystalline lens elevation

Lens surfaces were fitted by Zernike polynomial expansions (up to the 10th order) within a 5-mm optical zone. Figure 7 shows representative 2nd and 3rd order Zernike terms (astigmatism, coma and trefoil). Data are averages of 3 repeated measurements on each eye, and the error bars represent the standard deviation. Only fits corresponding to full distortion corrected surfaces are shown. The most relevant term was astigmatism at 0 and 90 deg (Z_2^2). Not correcting optical distortion produced an underestimation of the magnitude of astigmatism by 33% on average. Interestingly, all eyes showed vertical astigmatism in the

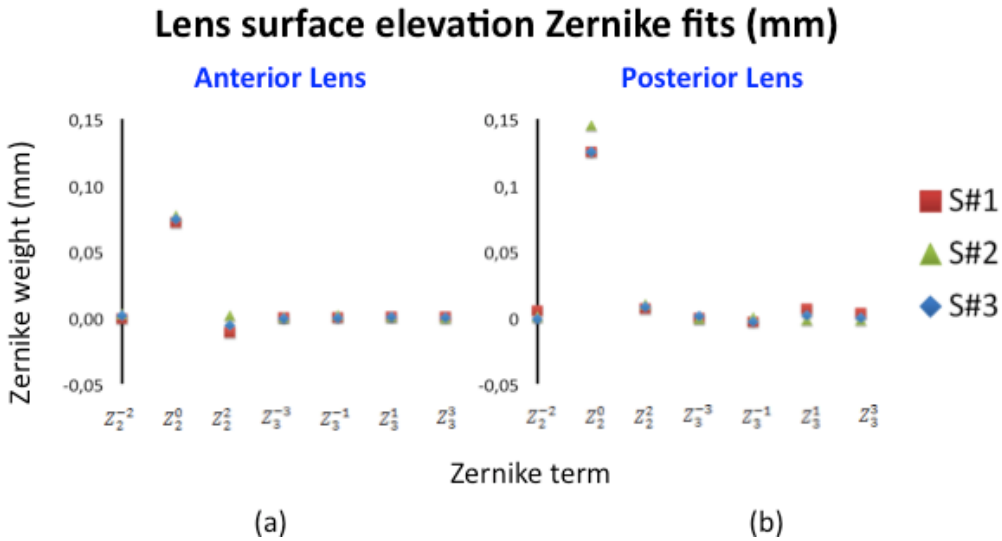

Fig. 7. Representative 2nd and 3rd order Zernike terms from the Zernike fit to full distortion corrected (a) anterior lens surface, and (b) posterior lens surface in 3 human lenses *in vivo*. Data are average values of 3 repeated measurements on S#1 (red squares), S#2 (green triangles), and S#3 (blue diamonds). Error bars are not represented since the error is smaller than the symbol. Data are for 5-mm pupils.

#170171 - $15.00 USD Received 7 Jun 2012; rev. 26 Jul 2012; accepted 24 Aug 2012; published 12 Sep 2012

anterior lens (negative Z_2^2, i.e. steepest vertical meridian), but a horizontal astigmatism in the posterior lens (positive Z_2^2, i.e. steepest vertical meridian).

Figure 8 shows elevation maps of the anterior and posterior lens surfaces in the 3 subjects of the study, within a 5-mm diameter zone. The elevation maps represent 10th order Zernike fits of the elevation maps relative to the best fitting sphere. The numbers below each map indicate the radii of curvature of best fitting sphere.

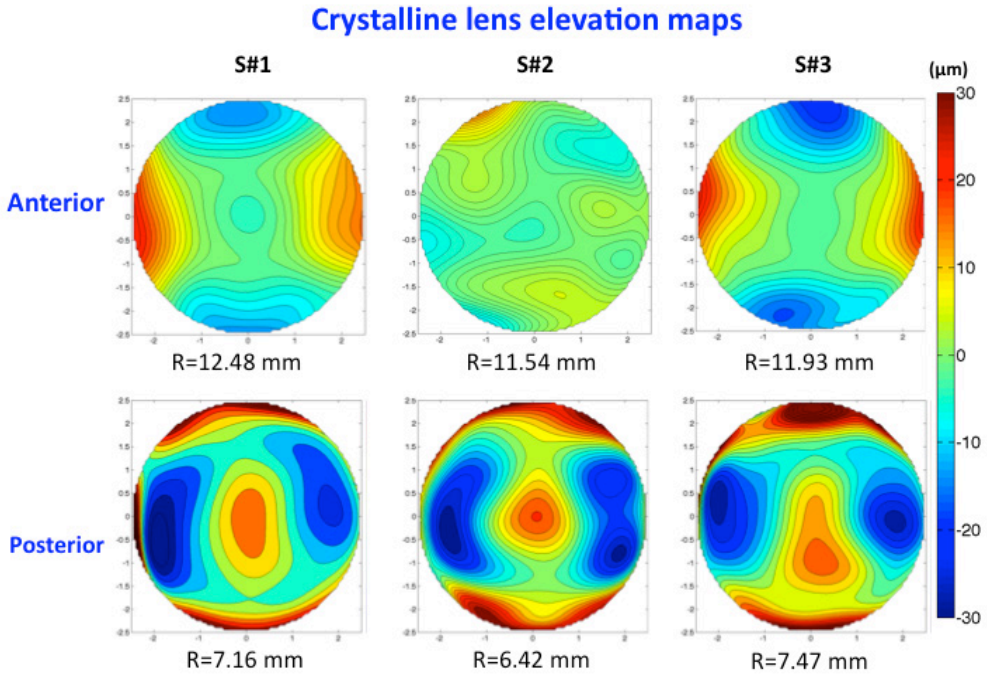

Fig. 8. Quantitative anterior (top) and posterior (bottom) crystalline lens elevation maps in 3 eyes *in vivo*, after full distortion correction. Maps are Zernike fits to the elevation maps, relative to the best fitting sphere. R = radii of curvature of the best fitting sphere (from fits to sphere quadrics). Data are for 5-mm pupils.

Figure 9 shows an illustration of the repeatability of the lens elevation maps in subject S#3, for both the anterior and posterior lens surfaces (5-mm optical zone). The numbers below each map represent the radii of curvature of best fitting sphere in mm. The average anterior lens radius of curvature was 12.02 ± 0.21 mm (1.7% of variability). The average posterior lens radius of curvature was 7.37 ± 0.09 mm, (1.2% variability). The average RMS lens elevation (relative to the best fitting sphere) was 2.08 ± 0.09 mm for the anterior lens (4% variability) and 9.92 ± 0.83 mm for the posterior lens (8% variability).

Additionally, in order to test the overall repeatability, the focal length of the eye was estimated by ray tracing through all reconstructed surfaces (cornea and crystalline lens). The estimated focal length ranged from 25.28 to 25.37 mm across repeated measurements in subject S#3, indicating within 1% repeatability.

#170171 - $15.00 USD Received 7 Jun 2012; rev. 26 Jul 2012; accepted 24 Aug 2012; published 12 Sep 2012

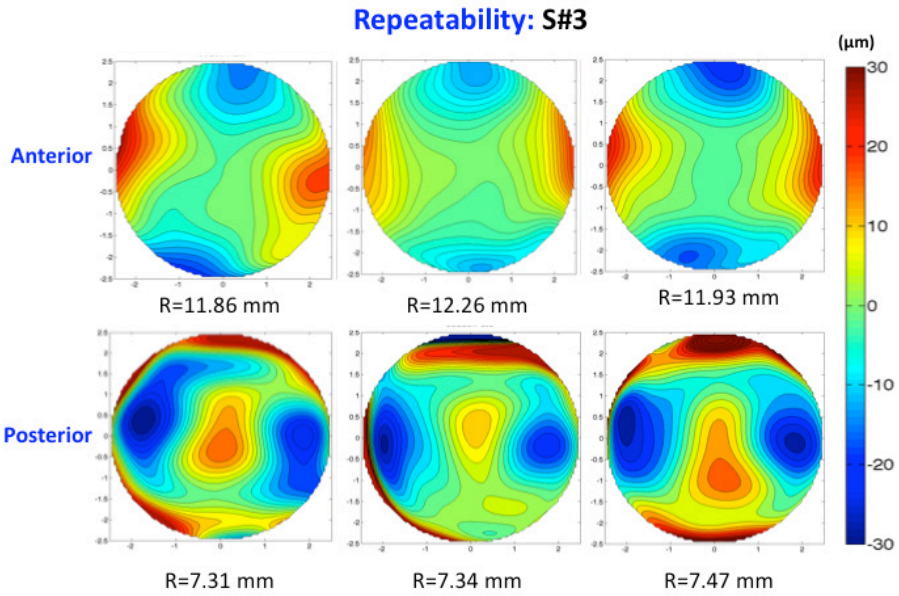

Fig. 9. Three repeated anterior and posterior lens surface elevation maps in subject #3. R = radii of curvature of the best fitting sphere (from fits to sphere quadrics). Data are for 5-mm pupils.

3.6. Crystalline lens thickness

Figure 10 shows lens thickness maps in the three subjects, estimated using uncorrected surfaces (obtained by simple divisions the optical distances by the average lens refractive index, and fan distortion corrections) and fully corrected surfaces (within a 5-mm diameter zone, centered at the pupil center). Central lens thickness was 3.18 ± 0.02mm for S#1, 3.36 ± 0.02mm for S#2, and 3.06 ± 0.04mm for S#3, and did not change with optical distortion

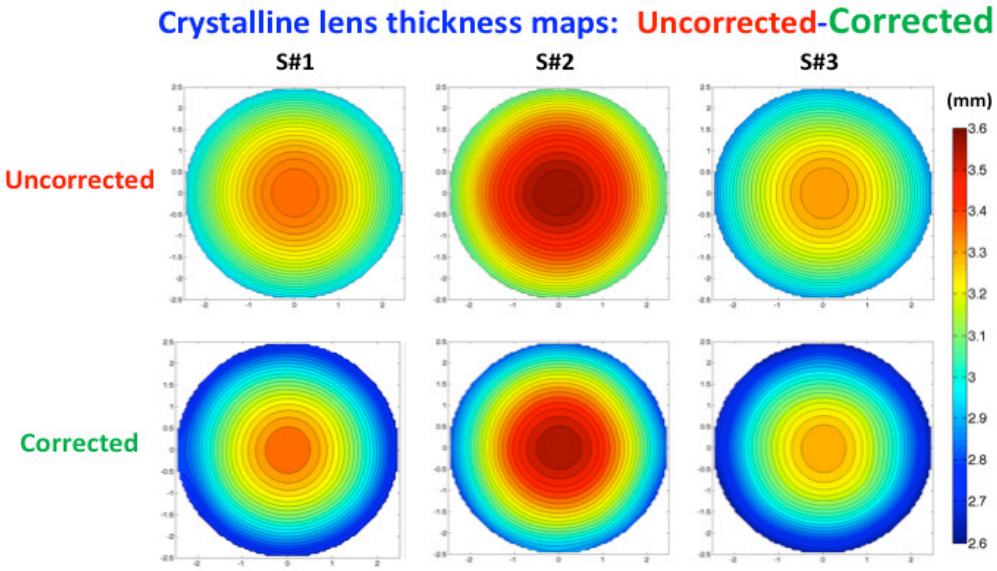

Fig. 10. Crystalline lens thickness maps obtained as direct subtraction from anterior to the posterior elevation maps, for uncorrected surfaces (top) and for fully corrected surfaces (bottom). Data are for 5-mm optical zone.

#170171 - $15.00 USD Received 7 Jun 2012; rev. 26 Jul 2012; accepted 24 Aug 2012; published 12 Sep 2012

correction of the surfaces. However, not correcting for optical distortion overestimated thickness by more than 15% on average in peripheral areas (2.5 mm from the center).

4. Discussion

We have presented a new methodology for obtaining accurate shape and 3-D topographies of the crystalline lens surfaces. To our knowledge, this is the first time that OCT has been applied to obtain quantitative 3-D geometry of the crystalline lens *in vivo*. The method has been tested using a model eye and a human donor lens *in vitro*, showing a good correspondence between nominal data of the model eye and the retrieved data after correction, and the posterior lens surface (obtained with the posterior lens surface facing the OCT beam) and the reconstructed posterior lens surface in the donor lens. The presented method builds on previous methods developed to obtain quantitative corneal elevation from OCT images [45,49], including fan and optical distortion correction [32,33,45,46,49], as well as image processing tools, which, along with newly developed routines for volume clustering (of cornea, iris, and lens), and 3-D merging and registration, allowed quantitative lens surface segmentation, correction and elevation. The lens surfaces were fitted by conicoids and biconicoids, as well as Zernike polynomial descriptions, which allowed estimates of the anterior and posterior lens radii of curvature, asphericity, astigmatism and high order irregularities.

Correction of optical distortion proved particularly relevant in the crystalline lens imaging, giving the accumulated refraction changes by multiple preceding surfaces, and the ray convergence. In keeping with theoretical predictions [46], correcting optical distortion improved accuracy in the estimates of the lens radii of curvature by 25% and 65% on average in the anterior and posterior lens respectively.

Most previous phakometric techniques were limited to the estimates of radii of curvature either from indirect measurements of light reflections from the lens surfaces (Purkinje imaging) or anterior segment imaging (such as Scheimpflug imaging). Our lens radii of curvature estimates *in vivo* (11.90 ± 1.34 mm for the anterior lens and 6.86 ± 0.63 mm for the posterior lens) fall within the ranges reported in the literature. Classical eye model [4] used 10 mm for the anterior lens and 6 mm for the posterior lens, whereas more recent models [54] used 12.4 and 8.1 mm respectively. Dubbleman et al. [16] reported an age-dependent expression for the anterior and posterior lens radius of human lenses *in vivo* based on corrected Scheimpflug measurements, which applied to the average data of our three subjects would predict 11.02-11.3 mm and 5.8-5.86 mm for the anterior and posterior lens radius respectively. Rosales et al. [20] in a comparative study of the crystalline lens radii of curvature estimated from Purkinje and Scheimpflug imaging on the same group of young subjects reported 10.8 mm and 11.1 mm, and 6.7 mm and 6.1 mm from each technique, for anterior and posterior lens radius of curvature respectively. Differences with respect to the OCT-based estimates may arise from the assumption of spherical surfaces in the Purkinje method [20], or the fit within a 3-mm optical zone in the Scheimpflug method [16], while we used a conic/biconic fitting within a 5-mm zone, and the reported radii of curvature correspond to the apical zone. Nevertheless, the intersubject variability (within the same age range than our three subjects) reported in previous studies is large: a range of 9-14 mm for the anterior and 4.7 –7 mm for the posterior lens radii in Dubbleman et al. [16]; 8.1-13.8 mm for the anterior and 5.1-7.15 mm for the posterior lens radii in Rosales et al. [20] in another study using Scheimpflug imaging, and 7.9-14.3 mm for the anterior and 5.2-8.65 mm for the posterior lens radii in Rosales et al. [21] using Purkinje imaging. The data reported in this study appear less variable across subjects, and well within the reported ranges.

To our knowledge, only Dubbleman et al. [16] reported lens asphericity measured *in vivo* from Scheimpflug imaging, also providing age-related expressions. The predicted asphericity from that study in the age range of our studies (–4.56 and –3.04 for the anterior and posterior lens surfaces, respectively) is significantly more negative than that obtained in the current

#170171 - $15.00 USD Received 7 Jun 2012; rev. 26 Jul 2012; accepted 24 Aug 2012; published 12 Sep 2012

OCT-based study (−1.31 ± 1.12 and −0.75 ± 0.83 for the anterior and posterior lens surfaces, respectively). However, the intersubject variability found by Dubbleman et al. [16] was extremely large (−20 to 7 for the anterior lens and −13 to 2 for the posterior lens). It is likely that the specific fitting method used by Dubbleman (two-stage fitting to a spherical surface followed by a fitting of the residuals to conic), the use of 2-D data sets, and the reported interactions between radius of curvature and asphericity in conic fits [55] play some role in the differences.

The 3-D acquisition and reconstruction of the lens surfaces with OCT allowed us to obtain 3-D lens geometry *in vivo*, for, to our knowledge, the first time in the literature. We had previously measured the 3-D geometry of crystalline lenses *in vitro* in the porcine [40] and human [56] lens. The correction of optical distortions from the cornea allowed reconstructions of lens surface topographies, very much like the conventional surface elevation of the cornea, widespread in the clinical practice. As our previous OCT-based corneal topographies, elevation measurements are based on a collection of regular B-scans, rather than meridians [47,48].

Unlike previous cross-sectional measurements of lens geometry which were limited to one meridian, 3-D measurements allow to investigate lens surface astigmatism. Very interestingly, the three subjects of our study show perpendicular orientation in the astigmatism of the anterior versus the posterior lens surface. To date, astigmatism of the crystalline lens *in vivo* is usually assessed by subtracting corneal from total aberrations [57–59]. Compensation of the corneal astigmatism by internal astigmatism has been postulated [59], as well as changes of this balance with age [59]. Measurements of the crystalline lens elevation *in vivo* will offer the possibility of investigating the sources of this compensation and potential age-related changes. In a previous study we investigated lens surface contribution to lens astigmatism in a porcine lens *in vitro*, and found that the lens gradient index of refraction (GRIN) may also play a compensatory role [40]. Undergoing research in our laboratory explores the role of GRIN in astigmatism and spherical aberration both in porcine and human lenses *in vitro*.

Our OCT-based crystalline lens elevation maps show minimal amounts of trefoil, coma or other high order aberrations. It is likely that the coma measured by direct subtraction of total minus corneal aberrations arises from the misalignment of the ocular components, including the off-axis position of the fovea [60,61]. Measurements of optical aberrations in isolated lenses using lateral images of the ray tracing in primate lenses [62], or by diffraction point interferometry [63] indicate presence of trefoil and other high order aberrations. The fact that the lens surface topographies are relative smooth suggests a contribution of the internal lens structure (likely line sutures) to the reported lens optical irregularities.

We provided the first report of lens surface shapes *in vivo* from OCT upon correction of optical (refraction) distortion, although (as previous reports based on Purkinje or Scheimpflug) we did not considered a GRIN in the lens. Borja et al. [41] suggested that the optimal refractive index for the correction of OCT images was closer to the average refractive index [37] than to the equivalent refractive index. In previous studies [41,44] we analyzed the potential effect of GRIN in the visualization and quantification of the posterior lens surface, and developed a tool for thru-GRIN optical distortion correction of OCT images, which we applied *in vitro* in 2-D. We concluded that using a homogeneous index of refraction as opposed to the actual lens GRIN profile did not produce significant discrepancies on the estimated radius of curvature, although it could overestimate the posterior lens asphericity in a 6 mm pupil diameter [41]. However, the results using a 4 mm pupil diameter [44] showed an improvement only in the RMS or peak to value differences. This result is consistent with the finding in a donor lens (now in 3-D) presented in the current study for validation. Estimates of the posterior lens surface elevation and lens thickness *in vivo* could therefore benefit slightly by increasing knowledge (and potential retrieval *in vivo*) of the lens GRIN.

#170171 - $15.00 USD Received 7 Jun 2012; rev. 26 Jul 2012; accepted 24 Aug 2012; published 12 Sep 2012

5. Conclusions

Anterior segment OCT provided with full distortion correction and automatic analysis tools allowed quantification of the human crystalline lens *in vivo* in 3-D. Correction of optical distortion is critical as simple division of the OCT optical distances by the refractive index produces an overestimation of the crystalline lens anterior and posterior radii of curvature by 25% and 65% respectively. The retrieved lens radii of curvature from OCT agree with phakometric data previously reported using Scheimpflug and Purkinke image along one meridian. We found slight negative lens surface asphericities, crossed astigmatism in the anterior and posterior lens surface, and low high order irregularities in the lens surfaces. OCT-based lens topography is a promising tool to investigate the lens optical properties, the contribution of the lens to the overall retinal image quality, and understanding the change of the physical properties of the lens with accommodation and aging.

Acknowledgments

The authors acknowledge funding from MICINN FIS2008-02065 and FIS2011-25637, EURHORCs-ESF EURYI-05-102-ES, ERC-2011-AdG-294099 and CEN-2091021 to S. Marcos.

#170171 - $15.00 USD Received 7 Jun 2012; rev. 26 Jul 2012; accepted 24 Aug 2012; published 12 Sep 2012